IEEE Access
Multidisciplinary | Rapid Review | Open Access Journal

Received July 2, 2019, accepted July 5, 2019, date of publication July 15, 2019, date of current version July 31, 2019.

Digital Object Identifier 10.1109/ACCESS.2019.2928948

Design of 3D Wireless Power Transfer System Based on 3D Printed Electronics

TAO HOU[1,2], JUN XU[2], WILLEMIJN S. ELKHUIZEN[2], CHARLIE C. L. WANG[3], (Senior Member, IEEE), JIEHUI JIANG[4], (Member, IEEE), JO M. P. GERAEDTS[2], AND YU SONG[2], (Member, IEEE)

[1]School of Mechatronic Engineering and Automation, Shanghai University, Shanghai 200444, China
[2]Faculty of Industrial Design Engineering, Delft University of Technology, Delft 2628 CE, The Netherlands
[3]Department of Mechanical and Automation Engineering, The Chinese University of Hong Kong, Hong Kong
[4]Shanghai Institute for Advanced Communication and Data Science, Shanghai University, Shanghai 200444, China

Corresponding author: Yu Song (y.song@tudelft.nl)

This work was partially supported by the Dutch NWO Next UPPS - Integrated Design Methodology for Ultra Personalized Products and Services project.

ABSTRACT 2D coil design limits the use of wireless power transfer (WPT) in many products with freeform outer shapes. In this paper, enabled by 3D printed electronics, we propose a systematic approach to design and fabricate 3D coils for WPT. Based on the circular spiral and rectangular spiral patterns, 3D receiver and transmitter coils can be generated on an arbitrarily selected region of a product and its offset, respectively. Mathematical models are proposed to estimate the self-inductance and the mutual-inductance of the 3D arbitrarily shaped coils for 3D WPT. This leads to a new design approach of a 3D WPT system. Several sets of 3D printed WPT systems were designed, simulated, and prototyped to demonstrate the effectiveness of the proposed design approach as well as the mathematical models. The calculation speed of the proposed mathematical models is 30 times faster than the simulation, and compared with the measurement results, the calculation results have mean absolute errors of 2.63% and 4.45% regarding the self- and the mutual-inductance, where the simulation results have mean absolute errors of 1.20% and 2.38%, respectively. Measurements also indicate that with a 5V input, the prototypes are able to deliver 1-watt power at an efficiency ranging between 20.9% and 25.3%. It was concluded that the proposed approach is feasible and promising for designing and manufacturing WPT using 3D printed electronics.

INDEX TERMS 3D coil, WPT, IPT, 3D printed electronics, design.

I. INTRODUCTION

Wireless power transfer (WPT), also known as wireless charging, attracted a wide range of attention in the past decade, mainly due to the rapid development of mobile technology and electrical vehicles [1]. Generally, techniques developed for WPT are advancing towards two directions: near-field (resonant) inductive coupling and far-field WPT by microwave. Compared to far-field techniques, near-field techniques have the advantages of higher efficiency and relatively lower frequency, which leads to fewer safety concerns. Currently, near-field WPT has already been widely adopted in the design of many products, e.g. the rechargeable toothbrush and the electrical vehicle [2].

The associate editor coordinating the review of this manuscript and approving it for publication was Ming Luo.

Inductive power transfer (IPT) is a popular working mechanism in near-field techniques where the QI standard [3] is a typical example. Traditionally, most IPT systems consist of a pair of mass-produced planar spiral coils connected to their two respective compensation networks. Recent developments of (consumer) product design introduces more 3D (freeform) outer shapes [4], as the visual appearance and usability play fundamental roles in the final decision of a customer when seeking congruency between price and functionality. This is especially true for personalized designs, where besides the form factors, rapid and accurate response to customers' demands is another key. These trends pose challenges to the designers of IPT as: 1) reducing possible lateral misalignment of two coils in the design, e.g. it is difficult to fully align the receiver coil in a rectangular-shaped phone to a circular charger; 2) reducing possible axial misalignment of

two coils, e.g. 3D forms may create a large gap between two embedded 2D planar coils; 3) increasing the transmitted power as there are limited planar areas to accommodate coils, e.g. the diameter of a QI charging coil is about 30 mm [3] and 4) Accelerating the design to production process, as for personalized products, each design may have its unique intrinsic properties.

Researchers and engineers tried different methods to tackle these challenges of embedding IPT in designs, for instance by adding more transmitter coils to the charging pad for tightly coupled systems [3]. Improving the quality factor of coils was also suggested to compensate smaller coupling factors in those scenarios [5]. In addition, the resonant WPT system was introduced to accommodate free positioning of products [4], [6]. However, such solutions usually lead to higher material cost, larger dimensions of the charging device, and/or reduced efficiency. In many cases, product designers have to sacrifice other features/functions for incorporating IPT in the design.

Recent development of 3D printed electronics offers new ways for designing and manufacturing IPT systems. Utilizing conductive materials in multi-material printing, 3D printed electronics [7] offers an extra dimension in designing and prototyping/manufacturing transmitter and receiver coils, i.e. those coils do not have to be planar. Using 3D coils, a large (projected) area can be utilized for IPT and a shorter distance between the transmitter and the receiver coils can be achieved. Both contribute to a more effective and efficient IPT.

In this paper, we propose a systematic approach for designing 3D transmitter and receiver coils that can be fabricated by 3D printed electronics, enabling a more effective and efficient IPT for freeform designs. Our main technical contributions are:

1. We proposed a new approach for designing 3D coils on an arbitrary 3D (freeform) surface for IPT;

2. We developed new mathematical models, which are extensions of current work, for calculating the self- and mutual- inductance of an arbitrarily shaped 3D coil(s); both the design approach and the models were verified by simulations and experiments, where prototypes were manufactured using 3D printed electronics.

The remainder of this paper is arranged as follows: First, literatures regarding the coil design of IPT, the methods for calculating self- and mutual- inductance of a coil(s), 3D printed electronics and its applications in WPT are presented. In Section III, the method of designing 3D coils is proposed based on Non-Uniform Rational B-Spline (NURBS) representations. Section IV describes the mathematical models for calculating self- and mutual- inductances of (a pair of) arbitrarily shaped 3D coil(s). The design and models were further verified by Finite Element Method (FEM) simulations (Section V) and experiments (Section VI). Different factors influencing the performance of the design, the model, the simulation and the manufacturing process are discussed in Section VII. Section VIII concludes the paper where future work is also highlighted.

II. LITERATURE REVIEW

A. COIL DESIGN FOR IPT

Generally, a simple IPT system consists of a power source, the transmitter (primary coil) and the receiver coil (pick-up coil), and their respective compensation networks, which include the primary and secondary circuits on the power and load side, respectively. The maximum transmitted power and the power transfer efficiency are crucial indicators in evaluating the effectiveness and efficiency of an IPT system. Key factors that influence these two key indicators are the design of the coils, the materials of the coils, the design of the compensation networks, etc. [5]

Given a simple IPT system where the transmitter coil and the receiver coil are directly connected to the power source and the load impedance, respectively, the maximal efficiency of the system can be described by $\eta_{max} = K_{12}^2 Q_1 Q_2 / \left(1 + \sqrt{1 + K_{12}^2 Q_1 Q_2}\right)^2$, and the maximum achievable energy in near-field coupled power-transfer system can be calculated as $P_{out-max} = K_{12} Q_1 Q_2 R_1 R_2 R_L V^2 / (R_1 (R_2 + R_L) + K_{12} Q_1 Q_2 R_1 R_2)^2$ [8]. Here K_{12} is the coupling factor between the transmitter and receiver coils, Q_1 and Q_2 are the quality factors of two coils. R_1, R_2 and R_L are the resistances of the transmitter coil, the receiver coil and the load, respectively. V is the voltage impinged on the primary side.

The coupling factor can be expressed as $K_{12} = M_{12} / \sqrt{L_1 L_2}$, where M_{12} is the mutual-inductance between the transmitter coil and the receiver coil. L_1 and L_2 are the self-inductance of these two coils, respectively. The value of the coupling factor is always between 0 and 1. The quality factor Q, which resembles a figure-of-merit of a coil [9], can be denoted as $Q = 2\pi f L / R$, where f is the frequency of the exciting current, L is the self-inductance of the coil and R is the resistance of the coil. In mass production, Q of a litz wire coil is typically 100 [10].

The power transfer efficiency of an IPT system is able to reach 70% to 80% [3]. Normally, a larger self-inductance of a coil indicates the potential of a higher quality factor of the coil. Together with larger mutual- inductances, the IPT system then has the potential of a high efficiency. Planar circular spiral coils and rectangular spiral coils are often used in the design of an IPT system. The advantage of using planar circular coils is that a pair of them has higher self- and mutual-inductances than square shaped coils regarding the same length of conductors [11]. But a rectangular spiral coil may have a larger inductive area compared with the circular spiral coil when the design is limited to a rectangular shape [12]. Coils in other shapes, e.g. elliptical coils, are also reported in the literature for specific applications [14]. Besides the properties of the coils, the mutual-inductances, and subsequently the coupling factor, can be significantly influenced by many

factors of practical usage scenarios, e.g. the angular, lateral and axial misalignments of these two coils. Misalignments often lead to a significant loss of magnetic flux during the power transfer, especially when the receiver coil is small [15]. In an example given by Hou *et al.* [16], the coupling factor of two coils in an IPT system may reduce 17 times due to large lateral misalignment, when compared to the most optimal alignment.

B. ESTIMATING SELF- AND MUTUAL- INDUCTANCE

Both the quality factor and the coupling factor are defined based on the resistances, the self- and/or mutual- inductances of the coils. The resistance of a coil can be calculated based on the geometry and the volumetric resistivity of the conductive material, e.g. the silver ink. For computing the self-inductance of a pair of 2D coils, many researchers had denoted frequency dependent formulas which consider the non-uniform current distribution in the coil and power loss on magnetic media [17], [18]. For instance, Sonntag *et al.* [19] proposed a method for estimating the mutual-inductance between two planar printed circuit board inductors featuring straight tracks. A new pseudo-analytical model for calculating DC inductance of flat circular inductors with rectangular cross section was proposed by Penalver *et al.* [20] Based on the partial inductance method, Tavakkoli *et al.* [21] proposed a new way to calculate the mutual inductance of two planar polygonal spiral coils with arbitrary number of sides. Researchers [22], [23] also derived the equations for calculating the self-inductance of the arbitrary shaped single-layer coils based on the shape functions.

Though most of research focused on 2D coils, researchers also paid attention on calculating of inductance of 3D coils. For example, Budnik *et al.* [24] developed a method to calculate mutual-inductance of 3D coaxial helical coils. Tominaka [25] derived an analytical expression for calculating the mutual-inductance of long coaxial helical conductors/solenoids from the Neumann's formula, and he also proposed a method for calculating the inductance of twisted conductors using the broken line approximation [26]. Sijoy and Chaturvedi [27] developed an efficient and accurate method for calculating the inductance of arbitrarily-wound helical coils. Volkmar *et al.* [28] proposed an algorithmic solution to calculate the inductance of a coil based on the Biot-Savart law. However, most of these methods were developed for calculating the inductance of the 2D planner coils or simple 3D coils. Moreover, literature research did not reveal any methods for calculating the self- and mutual-inductance of (a pair of) 3D arbitrarily shaped coil(s).

C. 3D PRINTED ELECTRONICS

Recently, various kinds of conductive materials have been introduced to 3D printing. The usage of both dielectric and conductive materials, i.e. 3D printed electronics, introduces another modality to the 3D printed designs, i.e. electric currents can flow through these conductive materials to transmit signals, to power actuators and/or to generate electromagnetic fields [29]. One of the first printers which is able to print electronic elements was the Voxel8 printer [30]. It adopts the multi-material Fused Deposition Modeling (FDM) [31] printing principle by utilizing Polylactic Acid (PLA) as the substrate material and the silver ink (or paste) as the conductive material. Additionally, a manual pick-n-place function is embedded in its printing procedure allowing for the incorporation of complicated electronics components in the prints. Similarly, the Aerosol Jet® system developed by Optomec® [32] is able to directly deposits conductive materials onto the (3D) substrate using the aerodynamic focusing technique. Several other techniques were also introduced for the construction of conductive connections (or traces) within a 3D structure as summarized by Mahto and Sniderman [29]. Among them, inkjet printing is another commonly used technique, e.g. the ElectroJet from ChemCubed [33]. The Nano dimension DragonFly™Pro [34]is another typical example which combines multi-material inkjet printing and nano-ink technology to build 3 μm thick layers with two materials (one nano-silver ink, one dielectric polymer ink).

In most of 3D printed electronics applications, the conductive ink (or paste) is one of the key enablers [35]. Today the nano-silver conductive ink is one of the most popular types of inks in 3D printing electronics, mainly due to its high conductivity and oxidative stability [36]. However, applications of the silver inks are still limited compared to using pure silver/copper/aluminum wires/traces in WPT, mainly due to its high resistivity. For instance, the volume resistivity (ρ, the reciprocal of conductivity) of the silver ink provided by Voxel8 is $3 \cdot 10^{-7}\Omega\cdot$ m [37], which is 16.8 times higher than that of the pure copper ($1.68 \cdot 10^{-8}\Omega\cdot$ m). Therefore in some applications, post-processing techniques were introduced after the "cold extrusion/printing" for better electrical/electromagnetic performance, e.g. annealing [38], hot-pressure sintering [39], laser sintering [40]. To further lower the resistivity of the conductive ink, researchers also introduced several methods to use molten metal as "inks". For instance, Océ Technologies [41] developed an inkjet printer which was able to dispense liquid metal droplets (up to 1800°C) through its printing heads.

D. APPLICATIONS OF 3D PRINTED ELECTRONICS IN WPT

Though the conductivity of silver inks is less than copper wires, the low fabrication cost and the ability of using flexible substrates attracted the attention of researchers and industry. 2D Printed electronics, i.e. single layer silver ink printing on various substrates, was introduced for designing low-power WPT systems earlier than for 3D designs. For instance, Jeong *et al.* [43] integrated a WPT system in a smartwatch strap using flexible 2D coils and magnetic field shielding materials.

3D printed electronics can offer more flexibility and capabilities in building complex objects with multiple mechanical and electronic functionalities, e.g. mouse, wireless sensors and gaming die [44]–[47]. Though most of 3D printed electronics applications focused on sensing systems with

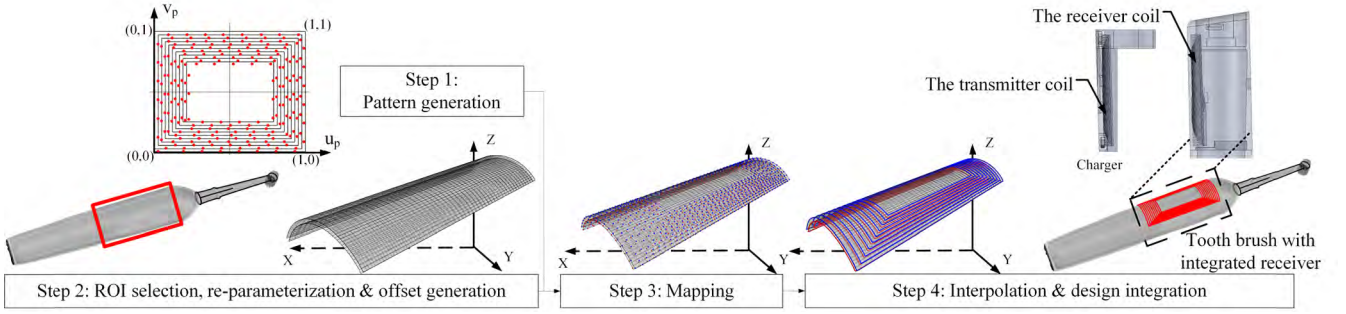

FIGURE 1. Design 3D coils for IPT.

embedded components [48], researchers also paid attention to the low-power IPT based on this newly developed technology. For instance, Yu *et al.* [49] used 3D additive manufacturing techniques to make electronics components, such as inductors, resistors, as well as circuits and passive wireless sensors. Recently Zhu *et al.* [50] developed an on-site 3D electronics printing technique to print sensors as well as a coil for WPT on human hands. Lazarus *et al.* [51] also incorporated conductive and magnetic materials into a 3D printed part for improving the inductance density as well as the power coupling for WPT. However, literature research did not reveal any systematic studies regarding the design, modelling and manufacturing of 3D coils for IPT. Meanwhile, product designers ask for such a tool to accelerate their design to manufacturing process, especially for embedding IPT in product designs with outer 3D (freeform) surfaces.

III. 3D COIL GEOMETRIC DESIGN

In our 3D coil design method, the planar spiral coil and the rectangular spiral coil are selected as patterns as for reasons listed in Section II. Given a Region-of-Interest (ROI) that represents (part of) a surface where the receiver coil will be located on/in the product, the design of 3D coils for IPT can be obtained in four steps as illustrated in Fig.1: 1) pattern generation - a circular spiral coil/rectangular spiral coil is selected as the pattern and the centerline of a coil is described as a NURBS curve in the parametric domain of a NURBS surface; 2) ROI selection, re-parameterization and offset creation - the ROI is re-parameterized using the NURBS representation. An offset surface, which resembles the location of the transmitter coil, is created, where the offset distance is specified based on the design requirements and characteristics of the coils; 3) mapping – a selected discretized pattern in the form of a sequential pointset are mapped to the two 3D surfaces, respectively; and 4) interpolation and design integration - by interpolating the mapped sequential pointset in both surfaces, the centerlines of the transmitter and the receiver coil are created, respectively. Based on the generated centerlines of the 3D coil, a minimal spiral growth rate is determined to maximize the performance as well as to avoid possible overlaps between adjacent traces. Both coils are then created by sweeping the designed cross-section of the coil along the centerlines. In the rest of this section, we present details of these four steps.

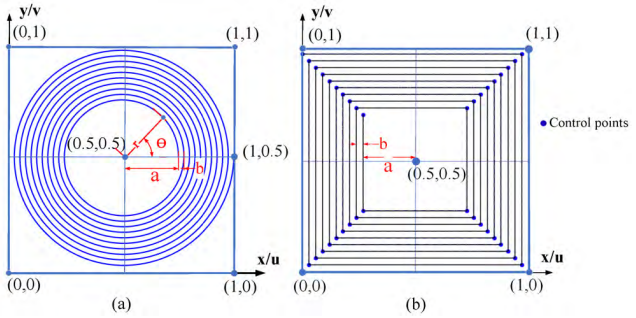

FIGURE 2. Patterns of 3D coils a: The circular spiral coil pattern; b: The rectangular spiral coil pattern.

A. PATTERN GENERATION

In a 2D plane, the centerline of a n-turn spiral coil (Fig.2(a)), which is enclosed by a 2D rectangle $RECT = \{Vertice_i \mid (0,0), (0,1), (1,1,), (1,0)\}$ (blue boundary in Fig.2(a)), can be described as:

$$C_{cs}(\theta) = \{(x,y) | 1/2 + (a + b\theta/2\pi)\, cos(\theta),\ 1/2 + (a + b\theta/2\pi)\sin(\theta),\ \theta = 0..2\pi n\} \quad (1)$$

where a and b are parameters that define the initial radius of the spiral and the distance between its adjacent turns (the spiral growth rate), respectively. As the *spiral* curve is enclosed by the rectangle $RECT$, relations between numbers of turns n and the initial radius a can be found as $a = (1 - 2(n-1)b)/2$. For the centerline of a planar rectangular coil, the representation is more complicated than the circular spiral curve. The corners of each turn of a rectangular spiral coil in the rectangle $RECT$ can be described as a sequential pointset (Fig. 2(b)):

$$RectCtp = \left\{(x_i, y_i) | \frac{1}{2} - \text{sign}\left(\frac{\pi}{4} + \frac{\pi}{2}i\right)\left(a + \text{floor}\left(\frac{i}{4} + 1\right)b\right), \times \frac{1}{2} - \text{sign}\left(-\frac{\pi}{4} + \frac{\pi}{2}i\right)\left(a + \text{floor}\left(\frac{i-1}{4} + 1\right)b\right), i = 0 \ldots n\right\} \quad (2)$$

where $2a$ is the starting width of the rectangle and b is the distance between two adjacent turns. As (2) only represents the corner points of the rectangular spiral pattern, to describe the complete pattern, we introduce a degree one NURBS curve [52] as:

$$\mathrm{C}_{rs}(\mathrm{u}) = \frac{\sum_{i=0}^{n} N_{i,p}(u)\,\omega_i RectCtp_i}{\sum_{i=0}^{n} N_{i,p}(u)\,\omega_i} \tag{3}$$

where $RectCtp_i$ are points on $RectCtp$. $p = 1$ and $\omega_i = 1$, which is the weight of each control point. $\{N_{i,p}(u)\}$ is the non-uniform rational B-spline basis function defined on the uniform knot vectors [52]. $u \in (0, 1)$, which is the parameter of the curve.

B. ROI SECTION, RE-PARAMETERIZATION & OFFSET GENERATION

If a designer wants to deploy the 3D receiver coil in (part of) a 3D surface(s) in the product, he/she may select this region as the ROI, which can be fitted with a NURBS surface $S_r(u, v)$ with a given accuracy (in our cases it was specified as 0.05 mm, which is a quarter of the resolution of the 3D printer). The transmitter coil will be located in $S_t(u, v)$, which is an offset of $S_r(u, v)$. In practice, the offset distance d is the sum of the thickness of the "walls" of the receiver and charging devices (with tolerance), and the positive and negative signs of d indicate an outward or an inward offset, respectively.

C. MAPPING

The transmitter and the receiver coils are created based on mapping the pattern (Equation (1) or (3)) to the ROI surface $S_r(u, v)$ and its offset surface $S_t(u, v)$, respectively. Using the principle of UV mapping [53], a selected pattern (e.g. Equation. (3)) can be discretized and mapped to $S_r(u, v)$ and $S_t(u, v)$ as two sequential pointsets $Coilpts_r = \{S_r(u_{kp}, v_{kp}) | kp = 0..m\}$ and $Coilpts_t = \{S_t(u_{kp}, v_{kp}) | kp = 0..m$, which resemble the centerlines of the transmitter and the receiver coils, respectively. It is worth mentioning that the UV mapping is not a linear mapping, i.e., the shape of the coils will be stretched and/or deformed according to the intrinsic properties of surfaces $S_r(u, v)$ and $S_t(u, v)$.

D. INTERPOLATION AND DESIGN INTEGRATION

Based on $Coilpts_t$ and $Coilpts_r$, centerlines of the receiver and the transmitter coils can be generated by interpolating these two pointsets to one-degree NURBS curves as $\mathrm{C}_r(\mathrm{u})$ and $\mathrm{C}_t(\mathrm{u})$. If the weight of every control point for $\mathrm{C}_r(\mathrm{u})$ and $\mathrm{C}_t(\mathrm{u})$ is 1, they can be simplified as:

$$\begin{aligned} \mathrm{C}_r(\mathrm{u}) &= \sum_{i=0}^{m} N_{i,p}(u)\, Coilpts_{ri} \quad u \in (0, 1) \\ \mathrm{C}_t(\mathrm{u}) &= \sum_{i=0}^{m} N_{i,p}(u)\, Coilpts_{ti} \quad u \in (0, 1) \end{aligned} \tag{4}$$

Figure 3 illustrates an example of the proposed approach where a spiral coil pattern is mapped to a 3D freeform surface. Though both patterns utilize a uniform growth rate, distances between each turn of coils are not uniform in 3D due to the properties of UV mapping. Therefore, to avoid possible overlap/collision of adjacent "spiral traces", it is crucial to find the smallest the distance between consecutive turns of both patterns. If the distance is less than the sum of the width of the coil and the resolution of the printer (for separating each turn), this turn will be removed.

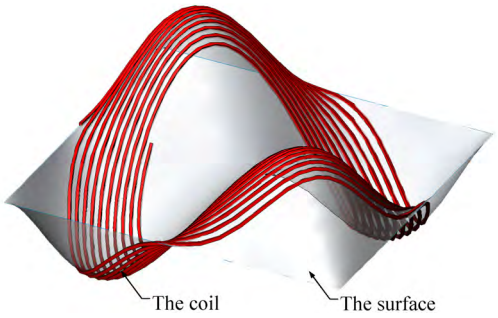

FIGURE 3. Example of a 3D coil on a 3D freeform surface.

To generate the 3D shapes of the coils, we sweep a rectangular profile, which resembles the cross section of the coil, along the curve to create the trace. The created solids can be integrated into 3D CAD designs, while the material is specified as the silver ink.

IV. SELF- AND MUTUAL- INDUCTANCE OF 3D COILS

In this section, new models for calculating the self-and mutual- inductance of an arbitrary 3D coil(s) are proposed based on the Biot-Savart law and existing work on calculating the self-inductance of a coil [25]. In the following, the proposed method is presented first with three steps. Based on this method, the calculation of multi-coil 3D transmitter(s) and receiver(s), which is designed to transfer larger power, is presented as well.

A. SELF- /MUTUAL- INDUCTANCE OF COILS

Given an arbitrary coil where $\mathrm{C}(\mathrm{u})$ is its centerline, its self-inductance can be calculated as the sum of the internal and the external inductances as:

$$L = L_{external} + L_{internal} \tag{5}$$

Here the internal inductance of the coil can be calculated from the magnetic energy within the coil as $L_{internal} = \mu_0/8\pi \int_0^1 \mathrm{C}(\mathrm{u})' du$ [54], where μ_0 denotes the magnetic permeability of the vacuum ($4\pi \cdot 10^{-7}$H/m).

Based on the method proposed by Tominaka [25], the external inductance of the coil can be approximated by the mean of the mutual-inductance ($M_{mid-inn}$) between the centerline and the inner edge of the coil, and the mutual-inductance ($M_{mid-out}$) between the centerline and the outer edge of the coil as:

$$L_{external} = (M_{mid-inn} + M_{mid-out})/2 \tag{6}$$

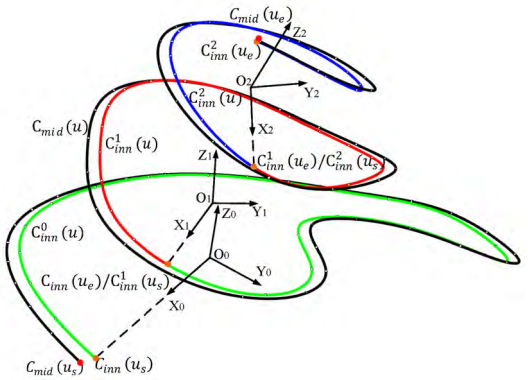

FIGURE 4. Finding turns of a 3D arbitrarily shaped coil.

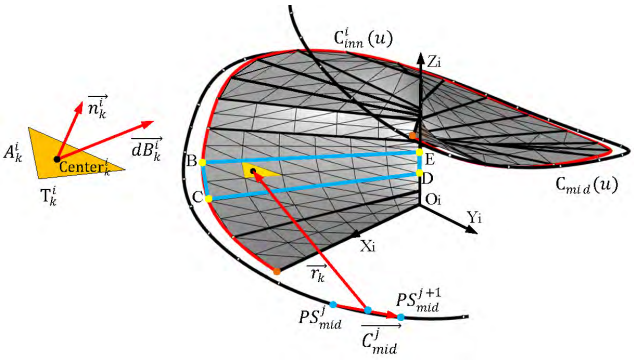

FIGURE 5. Calculating self- and mutual- inductance of a turn.

Given a 3D arbitrary shape coil, its $M_{mid-inn}$ and $M_{mid-out}$ can be calculated in 3 steps:

1) DIVIDE THE 3D CURVE INTO N TURNS

In this step, based on the concept of the loop model [25], a coil can be decomposed to N 3D turns (loops), where N is the number of turns of the curve. Figure 4 presents an example of this decomposition. Given a starting point $C_{inn}(u_s)$ of a NURBS curve $\{C_{inn}(u)|u \in (0,1)\}$, where u_s is a constant in the parameter space and $C_{inn}(u)$ is the inner edge of a coil, the end point of the first turn $C_{inn}(u_e)$ can be found as the second solution (the solution with the smallest Euclidean distance between two points) of

$$\frac{\partial \mathrm{D}(C_{inn}(u_s), C_{inn}(\mathrm{u}))}{\partial u} = 0 \tag{7}$$

where D is the Euclidean distance between point $C_{inn}(u_s)$ and curve $C_{inn}(u)$. If such a solution cannot be found, that means the previous turn is the end of the coil.

With the starting point $C_{inn}(u_s)$ and the ending point $C_{inn}(u_e)$, the first turn of the 3D coil can be represented as: $\{\mathrm{C}^0_{inn}(\mathrm{u})|u \in (u_s, u_e)\}$ as the green curve segment in Fig.4. A local Cartesian coordinate system of this turn can be established as $\mathrm{O_0X_0Y_0Z_0}$ (Fig.4). Its origin is defined as the geometric center of curve $\mathrm{C}^0_{inn}(u)$, the $\mathrm{X_0}$ and $\mathrm{Y_0}$ axes are located at the best fit plane of $\mathrm{C}^0_{inn}(u)$, where $\mathrm{X_0}$ is aligned along the projected line of $\mathrm{O_0}C_{inn}(u_s)$ on the best fit plane. Repeating this procedure, the second turn $\mathrm{C}^1_{inn}(u)$, the third turn $\mathrm{C}^2_{inn}(u)$ and their local coordinate systems can be established as the red, blue curves and $\mathrm{O_1X_1Y_1Z_1}$ and $\mathrm{O_2X_2Y_2Z_2}$ in Fig.4, respectively. Finally, $C_{inn}(\mathrm{u})$ can be approached as n+1 turns as $\{\mathrm{C}^i_{inn}(u)|i = 0..n\}$.

B. DISCRETIZE THE AREA OF EACH LOOP

The second step is to find the area enclosed by a turn of the 3D coil. For the inner edge of the i^{th} turn of a coil $\{C^i_{inn}(\mathrm{u})|u \in (u_{si}, u_{ei})\}$, it can be discretized to a pointset as $\mathrm{PS}^i_{inn}(\mathrm{u}) = \left\{\mathrm{PS}^{i,j}_{inn}|j = 0..m_{inn}\right\}$. Given two adjacent points $\mathrm{PS}^{i,j}_{inn}$ and $\mathrm{PS}^{i,j+1}_{inn}$ which are represented as point B and C in Fig.5, they can be projected to the Z-axis of the local coordinate system as point E and D, respectively. Using the segment of $\mathrm{C}^i_{inn}(\mathrm{u})$ between B and C, two lines BE and CD, and line DE along the local Z-axis, a NURBS surface $\{S_{BC}(u,v)|u,v \in (0,1)\}$ is created as the area enclosed by the blue lines in the figure. By tessellating surface $S_{BC}(u,v)$ along its u and v directions, a mesh with finite triangles can be generated as an approximation of the enclosed area where one of the triangles is highlighted in yellow (Fig.5). Repeating this step for all adjacent points $PS^{i,j}_{inn}$ and $PS^{i,j+1}_{inn}$ in this turn, the enclosed area of this 3D turn $\mathrm{C}^i_{inn}(\mathrm{u})$ can be represented as a triangular mesh $Mesh_i = \{T^i_k|k = 0\ldots h_i\}$, where T^i_k is a triangle in the mesh, its geometric center can be represented as $Center^i_k$, its area is A^i_k and its normal direction is $\overrightarrow{n^i_k}$.

C. CALCULATE THE MUTUAL INDUCTANCE

The mutual-inductance between C_{inn} and C_{mid} can be approximated as:

$$\mathrm{M_{mid-inn}} = \oint_{\mathrm{A}} \frac{\Phi_{\mathrm{A}}}{\mathrm{I}} = \oint_A \overrightarrow{dB} \bullet \overrightarrow{dA}/I \tag{8}$$

where $\overrightarrow{dB}$ is the magnet flux that induced by C_{mid} and crossed the enclosed area of C_{inn}, A is the enclosed area of the C_{inn} and I is the current. Using the Biot–Savart law, $\overrightarrow{dB}$ can be defined as $\overrightarrow{dB} = \int_{\mathrm{Cmid}} \frac{\mu_0 I \overrightarrow{dC_{mid}} \times \overrightarrow{r_k}}{4\pi |r_k|^3}$, where $\overrightarrow{r_k}$ is the distance vector between $\overrightarrow{dA}$ and $\overrightarrow{dC_{mid}}$.

Given C_{mid} as a curve $\{C_{mid}(u)|u \in (0,1)\}$, it can be discretized as a point set $PS_{mid}(\mathrm{u}) = \left\{PS^j_{mid}|j = 0..m_{mid}\right\}$. As the enclosed area of each turn is discretized to $T^i_k|k = 0\ldots h_i$, for $C_{inn}(\mathrm{u})$, $M_{mid-inn}$ can be approximated as:

$$M_{mid-inn} = \frac{\mu_0}{4\pi} \sum_{i=0}^{n} \sum_{\mathrm{j}=0}^{m_{mid}} \left(\sum_{\mathrm{k}=0}^{h_i} \left(\frac{\overrightarrow{C^j_{mid}(u)} \times \overrightarrow{r_k}}{r_k^3} \right) \bullet A^i_k \overrightarrow{n^i_k} \right) \tag{9}$$

Here $\overrightarrow{C^j_{mid}} = PS^{j+1}_{mid} - PS^j_{mid}$, which is an approximation of a segment of $C_{mid}(u)$, $\overrightarrow{r_k} = Center^i_k - (PS^{j+1}_{mid} + PS^j_{mid})/2$, which is the distance between the center of the triangle T^i_k and $\overrightarrow{C^j_{mid}}$. Besides, $\overrightarrow{n^i_k}$ is defined as the normal direction of the triangle and it is used to calculate the projection area of A^i_k perpendicular to the magnetic field $\overrightarrow{dB^i_k}$.

Similarly, $M_{mid-out}$ can be calculated using (9) as well. Then the external inductance $L_{external}$ can be found based on the average of the sum of $M_{mid-out}$ and $M_{mid-\text{inn}}$ as (6). Consecutively, the self-inductance L of the coil can be found using (5). For calculating the mutual-inductance of arbitrarily shaped two 3D coils, Equation (9) can also be used by replacing $C^j_{mid}(u)$ as the centerline of one coil and C^i_{inn} (u) as the centerline of another coil, respectively.

D. MULTI-COIL TRANSMITTER/RECEIVER

In many designs, it is difficult to design a large enough coil to transfer the needed power due to geometric and manufacturing constrains [55]. A possible solution is to connect multiple small coils in either/both side(s) of the transmitter or/and the receiver to increase the self-inductance of the transmitter/receiver coil(s) and therefore to increase the power that can be transmitted.

Given a multi-coil which consists of n small coils in a series connection, the self-inductance of the multi-coil can be found as $L_{series} = \sum_{i=1}^{n} L_i + 2\sum_{i=1}^{n-1}\sum_{j=i+1}^{n} M_{ij}$. Here L_i is the self-inductance of the i^{th} small coil (Equation (6)) and M_{ij} is the mutual- inductance between the i^{th} and the j^{th} coil. For the mutual-inductance between the transmitter coils (n small coils) and receiver coils (m small coils), it can be calculated as $M_{multi} = \sum_{i=1}^{n}\sum_{k=1}^{m} M_{i,k}$, where $M_{i,k}$ is the mutual-inductance between the i^{th} coil of the transmitter and the k^{th} coil of the receiver coil.

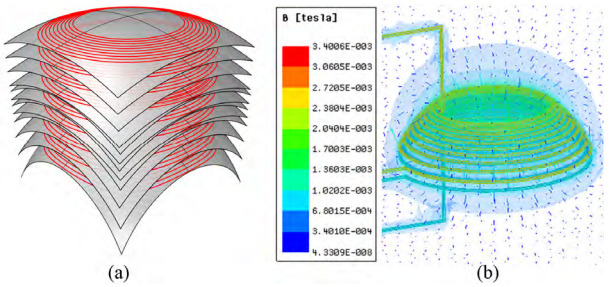

FIGURE 6. Simulation setups and results a: Pattern mapped to the ROIs; b: Simulated B field of the IPT system.

V. SIMULATION

To evaluate the proposed approach, we designed a set of 3D coils based on the method proposed in Section III and evaluated their performance using the proposed model (Section IV) as well as the ANSYS$^{\text{TM}}$Maxwell$^{\text{TM}}$simulation tool. In the designs, a series of ROIs were created by projecting the same rectangle (66 mm × 66 mm) along z-axis to different hemispherical surfaces with different radii (range from 50 to 105 mm with a 5 mm step, shown in Fig.6(a)). Then the transmitter coil was designed by mapping a 10-turn circular spiral pattern to each ROI. For each receiver coil, its receiver coil was created by mapping the same pattern to a 2 mm offset (not shown in Fig.6(a)) of the ROI. In addition, the receiver coil can be moved along the z-axis from 0 to 15 mm (1 mm per step) to simulate the axial misalignment. The varying radii of the hemisphere and the simulated axial misalignment resulted in 192 setups in the calculation and the simulation.

The mathematical models were implemented by Python using the NumPy and the NURBS python library. In the simulation, we used the magnetostatics analysis with a 2A current at 100 KHZ, which is a typical input following the QI standard [3]. Figure 6(b) presents the simulated B field of one of these setups. With an Intel$^{\text{TM}}$Core i5$^{\text{TM}}$ 3.7GHZ CPU, it took about 7 minutes to simulate each setup, which resulted in a total 1344 minutes computing time. This was much longer than the computing time of using the proposed mathematical models, which cost 14 seconds for each setup and 44.8 minutes for all setups using the same computer (30 times faster).

In Fig.7, the simulated self-inductance is compared to the results calculated by the proposed mathematical models. It can be found that self-inductances calculated by the mathematical model is larger than the simulation in both cases. The mean absolute error is $2.3 \cdot 10^{-7}$ H, which accounts for 3.25% of the average of the simulation results. The figures also show that, the self-inductance of the circular spiral coil decreases when the radius increases from 50 mm to 105 mm.

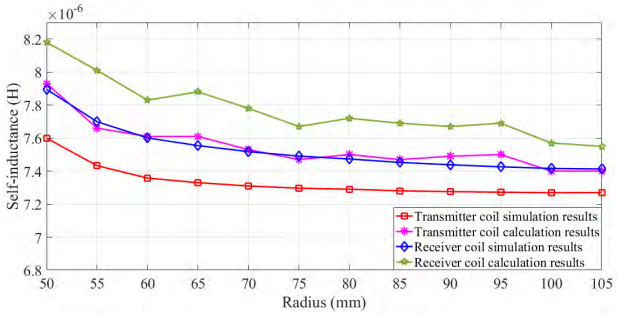

FIGURE 7. Calculation and simulation results of the self-inductance of 3D coils on hemispherical surfaces with different radii.

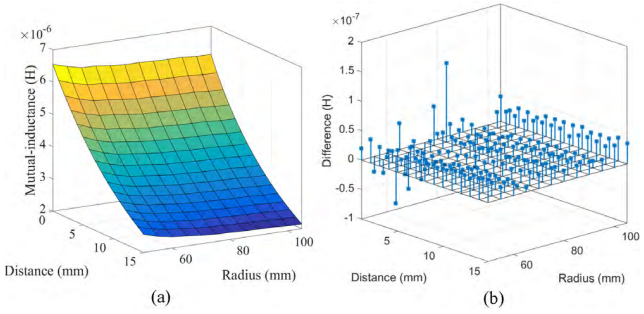

FIGURE 8. Mutual-inductances of coils a: Simulation results; b: Comparing the calculation results to the simulation results.

Figure 8 presents a comparison of the calculated and simulated mutual-inductance of two pairs of coils, respectively. In Fig.8(a), the simulation results of the mutual-inductance against the radius of the hemispherical surface (varying from 50 to 105 mm) and the movement of the transmitter coil along the Z-axis (axial misalignment, varying from 0 to 15 mm)

are presented. It can be seen that the axial misalignment has a much larger influence on the mutual-inductance than the radius of the hemisphere. Figure.8(b) shows the errors between the calculation and the simulation. The mean absolute error between the calculation and simulation is $1.9 \cdot 10^{-8}$ H, and on average the calculation result is 1.6% larger than the simulation result.

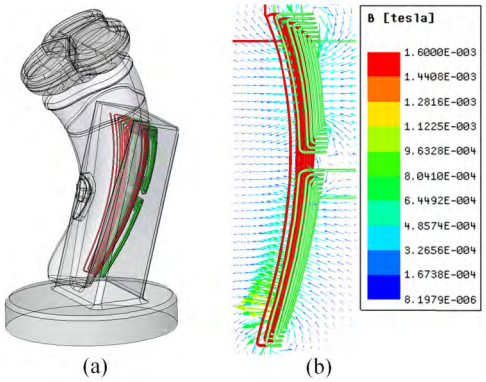

FIGURE 9. Multi-coil IPT a. The design of the multi-coil IPT system where two coils are connected in series as the transmitter (green) and a single coil (red) is used as the receiver; b. Simulation results.

Figure 9 presents the simulation results of the design of a shaver with a multi-coil WPT system. In the system (Fig.9(a)), the transmitter coil consists of two small coils (green) where the receiver only has a large coil (red). The calculated self-inductance of the multi-coil is $1.28 \cdot 10^{-5}$ H, and the mutual-inductance between the transmitter and receiver coil is $9.26 \cdot 10^{-6}$ H where for the simulation, the values are $1.25 \cdot 10^{-5}$ H and $9.18 \cdot 10^{-6}$ H, respectively. Simulation results are in accordance with the calculation results, and the error is less than 5%.

VI. EXPERIMENTS

To further verify the performance of the proposed approach for designing 3D WPT system, two sets of circular spiral coils and two sets of rectangular spiral coils were printed using a Voxel8 printer. In the 3D prints, the PLA was used as the substrate and the Voxel8 silver ink was used as conductive material. It has a density of 3700 kg/m^3 and the volume resistivity is below $3 \cdot 10^{-7}$ Ω· m. According to its specification, it will take approx. 12 hours to dry at room temperature to get 90% of the specified conductivity [37]. In practice, we dried it for more than 24 hours for a better performance. The adhesion strength between the silver ink and the PLA is approx. 4-5 based on the tape test of ASTM [56]. The dried silver ink was able to withstand small deformation as the strain of the silver trace at electrical break is 5% [56].

In Fig.10(a), the printing process of a 3D rectangular spiral coil is presented. Figure 10(b) presents four sets of coils with different 3D shapes. For a better visualization, those coils were not embedded in the design, therefore silver traces can be observed directly. Table 1 presents the measurement results of these four sets of coils. In the Table, T represents the

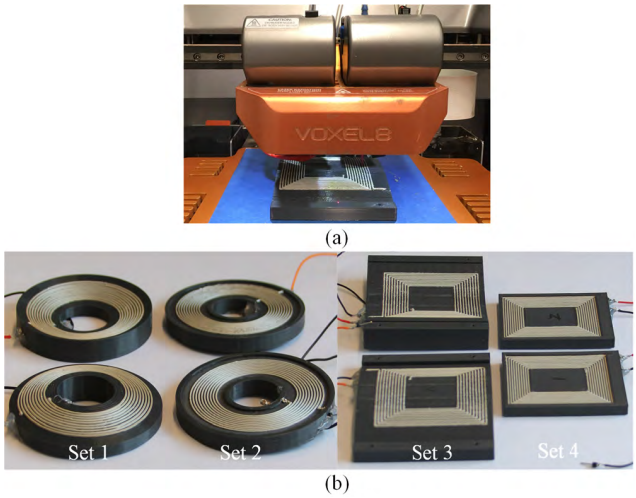

FIGURE 10. 3D coils fabricated by 3D printed electronics a: Printing a 3D rectangular coil; b: Set 1 – 3D circular coils on hemispherical surfaces, Set 2 – 2D planar circular coil, Set 3 – 3D rectangular coils on cylindrical surfaces, Set 4 – 2D planar rectangular coils.

transmitter coil and R represents the receiver coil. Regarding the resistances, for Set 1 and Set 2, the values are about 1.4 Ω and for Set 3 and Set 4, the resistances are about 1.6 Ω. For both the circular spiral coils and the rectangular spiral coils, the measurements of self-inductances are close to the results of calculation and simulation. All coupling factors are above 0.7, which indicates the potential for a high efficiency IPT system. The quality factors of all the four pairs of coils are not high, mainly due to the large resistances introduced by the silver ink.

Using the measurement method (Fig.11(a)) recommended by the Wireless Power Consortium [57], we measured the actual power transfer efficiency as $\eta = V_2A_2/V_1A_1$. In the experiment, the input power was about 5 Watt and a 10 Ω resistive load was deployed on the receiver side. No electromagnetic shield was used for the IPT. The measured power transfer efficiency of the 4 sets of coils were 21.8% (3D circular spiral coils on the hemispherical surface with a radius of 100 mm), 22.6% (2D circular spiral coil), 25.3% (3D rectangular spiral coil on the cylindrical surface with a radius of 100 mm) and 25.1% (2D rectangular spiral coil) respectively. It is worth mentioning that the power consumption of the circuits of the transmitter and the receiver were included in all measurements as well.

To further verify the possibility of using 3D coils in product design, we redesigned the 3D IPT system for an electric toothbrush using the proposed approach and printed a prototype using the Voxel8 printer. In this new design, the receiver coil is embedded in the shell of the toothbrush and the transmitter coil is embedded in the holder. Figure 12(a) and Fig.12(b) show intermediate steps in printing the transmitter (and the holder) and the receiver coils (and the shell), respectively. Figure 12(c) presents the prototype. The power transfer efficiency between the coils in the holder and the shell was measured as 18.6%, which was slight lower than the printed

TABLE 1. Measurement results of 4 sets of coils.

	Circular spiral coils				Rectangular spiral coils			
	Set 1 (R=100 mm)		Set 2 (R=∞)		Set 3 (R=100 mm)		Set 4 (R=∞)	
	T	R	T	R	T	R	T	R
Resistance(Ω)	1.4	1.4	1.4	1.5	1.6	1.5	1.6	1.6
Self-inductance(μH)	7.23	7.40	7.22	7.30	7.01	7.06	6.90	6.95
Calculation error	2.3%	3.2%	4.1%	3.0%	4.2%	2.3%	1.3%	0.6%
Simulation error	-0.6%	0.4%	0.4%	0.7%	1.9%	2.2%	2.1%	1.3%
Mutual- inductance(μH)	5.63		5.52		5.39		5.19	
Calculation error	3.1%		5.6%		3.8%		5.3%	
Simulation error	3.0%		2.5%		2.9%		1.1%	
Quality factor	3.24	3.32	3.23	3.06	2.75	2.96	2.71	2.73
Simulation error	11.2%	13.2%	11.1%	13.8%	3.5%	10.3%	3.6%	3.6%
	T→R	R→T	T→R	R→T	T→R	R→T	T→R	R→T
Coupling factor	0.77	0.7	0.76	0.76	0.79	0.78	0.75	0.75
Calculation error	0.2%	1.2%	2.0%	2.0%	1.7%	3.8%	4.3%	4.3%
Simulation error	2.5%	3.8%	1.9%	1.9%	-1.1%	1.3%	-0.6%	-0.6%
Power transfer efficiency	21.8%	20.9%	22.6%	22.6%	25.3%	23.7%	25.1%	25.1%

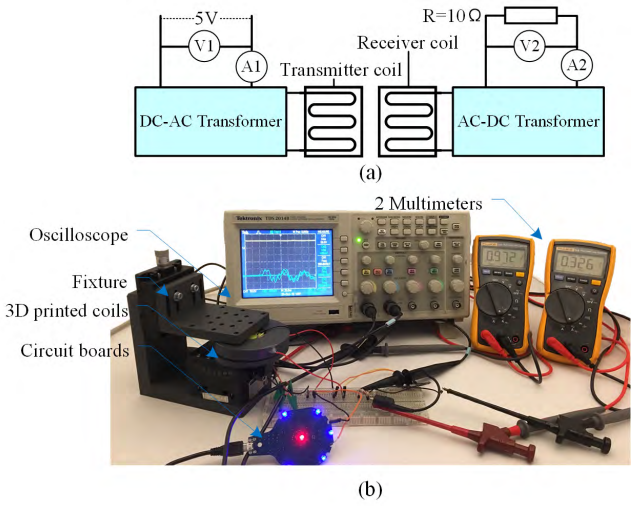

FIGURE 11. Measurements for the 3D coils a: Schematic of the measurement circuit; b: Measuring the power transfer efficiency.

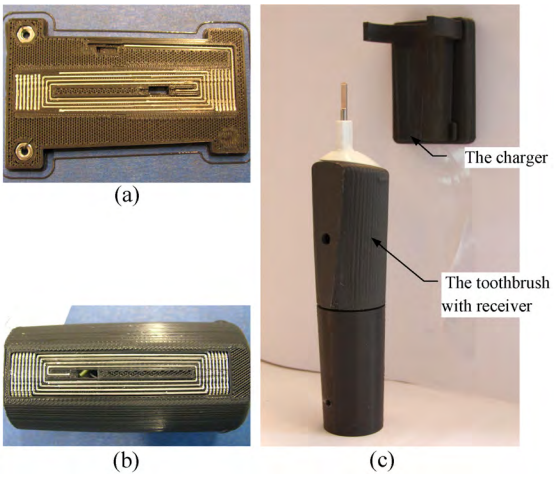

FIGURE 12. The newly designed electrical toothbrush embeds a 3D IPT system a: An intermediate step in printing the charger; b: An intermediate step in printing the receiver; c: 3D printed toothbrush that embeds a 3D IPT system.

4 sets of coils. The major reason was that the thickness of the shell was increased (around 2.5 mm) for better mechanical properties.

VII. DISCUSSION

A. DIRECTIONAL POWER TRANSFER EFFICIENCY

In our design, a same pattern is mapped to an ROI and its offset to form the centerlines of the transmitter and the receiver coils, respectively. As the geometries of the ROI and its offset are different, the shapes of the two coils are different as well. Generally, using a small coil as the transmitter, the power transfer efficiency is higher than using the larger coil, as the large coil encloses the small coil and is able to capture more electromagnetic energy radiated by the transmitter. Experiment results also proved this as the coupling factors from the smaller coil to the larger coil were slightly larger (in average 2.6%) in both Set 1 and Set 3. Therefore, it is preferred to use the smaller coil as the transmitter in the design of a 3D IPT system.

B. CALCULATION, SIMULATION AND EXPERIMENT RESULTS

In general, measurement results regarding the self-inductance, the mutual-inductance and the coupling factor of coil(s) were slightly lower than the simulation, and the calculation was the highest. For instance, regarding the self-inductances, the mean absolute errors of the calculation and the simulation regarding the measurement are 2.63% and 1.20% higher, respectively. And for the mutual-inductance, the mean absolute errors are 4.45% and 2.38% higher, respectively. These errors can be explained by multiple factors. First, for accelerating the speeds of the calculation and simulation, we set surround environment of the coil as vacuum, and in the experiment, those coils were printed on the PLA substrate surrounded by the air. Though the magnetic permeabilities of the PLA, the air and the vacuum are similar, there are slight differences and errors were introduced. Secondly, the silver traces were treated as solid lines with uniform cross-sections in the calculation and the simulation. However, in the

3D printed coils, it cannot be guaranteed. Details of the limitations of the manufacturing process will be discussed in the next section. Regarding the difference between the calculation and the simulation, the skin effect, which might influence the results, was taken into consideration in the simulation [58], but not in the calculation. For instance, the mutual-inductance were calculated based on the centerline and edges of the coil, however, the current density might be different in those locations due to skin effect.

Though there were errors in the calculation and the simulation, the absolute mean errors were consistent and were below 5%. Considering the cost of the prototype and the speed of the simulation (30 times slower than the calculation), the models that developed in this paper are useful tools for estimating the coil properties for designing a WPT system, especially in the design exploration and design optimization, where many iterations of calculation might be needed.

C. MANUFACTURING PROCESS

The effectiveness and efficiency of an IPT strongly depends on the resistance of the coil, the coupling factors (k) between the coils and their quality factors (Q). For the resistances of the prototypes, all measurements are higher than the simulation.

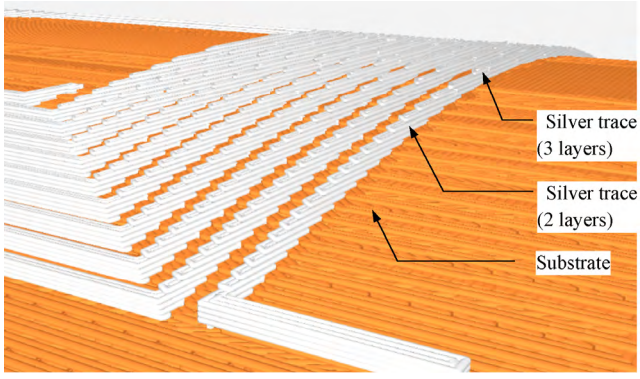

FIGURE 13. Toolpath for printing a 3D coil.

This can be explained by the nature of the 3D printing process. The ''cold'' extruded silver ink has a round shape, and the fragments of inks are stacked together to form the conductive trace that is higher than the thickness of the extruded ink. It is inevitable that extra resistance will be introduced and this was especially true for traces with large inclination angles regarding the building plane, as the number of building layers for each segment of a trace may vary according the angle. Figure 13 shows the toolpath for printing a silver coil where the height of the coil is designed as 3 horizontal layers. It can be seen that the silver trace fragments are ''stacked'' on each other in different layers to approximate the traces on the curved surface. In some cases, only 2 layers are available as the thickness is discretized according to the resolution of the printer (0.19 mm). This also introduces extra resistances.

In the proposed research we increased the thickness of the trace to guarantee that the ''minimal'' number of layers of silver in the toolpath. Researchers also proposed different methods to reduce the resistance. For instance, Kim *et al.* [59] demonstrated the possibility of connecting multiple layers by inserting metal connector between them in in the printing process. Angel *et al.* [60] proposed a new curing method for parts printed on a uniaxial double sloped 3D surface by photonic sintering. Hawasli *et al.* [61] also demonstrated that the resistances of 3D printed traces can be lowered by using a combination of photonic sintering and copper electroplating.

Our experiments indicated that the bond between the conductive ink and the substrate material (ASTM Tape Adhesion: 4-5 [56]) were able to support the usage of the WPT system. To further improve the adhesion, the metal ink proposed by Yung *et al.* [62] could be considered. Silane coupling agents suggested by Lee *et al.* [63] can be considered as well.

D. THE QUALITY FACTORS (Q)

Though calculation, simulation and experiments indicate the potentials of high efficiency of the proposed 3D design, the quality factor of the coils are around 3, which is not high compared to conventional wireless charging coils. And it is also the major reason for the relatively low efficiency. However, the 3D design might already be used to charge/power devices that has limited power requirements, for instance, electrical toothbrush, sensors for Internet of Things (IoT) applications, and biosensors [49].

For applications where large currents are needed, the quality factor can be further improved by decreasing the resistance of the coils, for instance by enlarging the cross-section area of a trace; designing more parallel traces in available space; improving contact between traces and/or, using inks with better conductivity. Although theoretically enlarging the cross-section area could reduce the resistance, due to the skin effect, the improvement is likely to be limited. 3D designs offer more available space to accommodate parallel traces, but the number of traces also depends on the printing resolution. At current stage, the resolution of the Voxel8 is about 0.19 mm (layer height), which makes it difficult to reach the same number of strands as a litz wire. The volume resistivity of the silver link used in this research, is approximately $3 \cdot 10^{-7} \Omega \cdot$ m, which is 17.2 times larger than that of the pure silver ($1.65 \cdot 10^{-8} \Omega \cdot$ m). Besides methods discussed in previous section, if a metal-jet [41], which is able to print pure silver with higher resolution, is used, the quality factor of a coil could be greatly improved from $\sim$3 to $\sim$55.

E. LIMITATIONS

In the proposed research, we limited our discussion on the design and manufacturing of 3D coils. Topologies of the compensation network, e.g., SS, SP, PS and PP, were not discussed. The use of metamaterial with negative permeability and permittivity is to be investigated as well [64]. Additionally, we mapped patterns as close as possible to the boundary of the ROI for a better performance of the 3D IPT. For complicated freeform surfaces, more study is needed to investigate the optimal orientation of (each turn of) the

coil regarding the self- and mutual- inductance of the coils. Regarding the materials, further study on the curing methods, as well as the adhesion of the silver trace on surfaces with different inclination angles and different textures, are needed.

VIII. CONCLUSION

In this paper, a systematic approach of designing, modelling and manufacturing 3D coils for IPT is presented based on 3D printed electronics. Two patterns are proposed as the basic shapes of the 3D coils. Using UV mapping, these patterns can be mapped to an arbitrarily selected region of a product and its offset surface to generate 3D transmitter and the receiver coils, respectively. Self- and mutual- inductances of the 3D coils, as well as the efficiency of the IPT system, can be directly calculated using the proposed mathematical models. The design and the mathematical models were further verified by simulation and experiments, where two sets of circular spiral coils and two sets of rectangular spiral coils were designed based on the proposed method and manufactured by 3D printed electronics. It is concluded that the proposed approach is feasible and promising for manufacturing IPT using 3D printed electronics.

Current work is directed towards further improvements of the design approach and the performance of the coils. More complicated freeform surfaces will be studied for utilizing the proposed approach in more designs. Regarding the quality factor (Q) of the coils, different types of conductive inks, the spatial arrangement of the conductive traces and the manufacturing methods are being investigated. The possibility of printing ferrite materials as electromagnetic shields will be explored as well.

ACKNOWLEDGMENT

The author would like to express their appreciation to Miss Tessa T.W. Essers, Mr. Joris van Dam, Mr. Adrie Kooijman and Mr. Roy A. Boekraad for their kind help in the prototyping/manufacturing.

REFERENCES

[1] H. Lakhal, M. Dhieb, H. Ghariani, and M. Lahiani, "Wireless power transmission technologies and applications," in *Proc. 14th Int. Conf. Sci. Techn. Autom. Control Comput. Eng.*, Sousse, Tunisia, Dec. 2013, pp. 168–173.

[2] G. A. Covic and J. T. Boys, "Inductive power transfer," *Proc. IEEE*, vol. 101, no. 6, pp. 1276–1289, Jun. 2013.

[3] Wireless Power Consortium. (2019). *What is Wireless Charging*. Accessed: Jun. 19, 2019. [Online]. Available: https://www.wirelesspowerconsortium.com

[4] E. Waffenschmidt, "Homogeneous magnetic coupling for free positioning in an inductive wireless power system," *IEEE J. Emerg. Sel. Topics Power Electron.*, vol. 3, no. 1, pp. 226–233, Mar. 2015.

[5] Z. Zhang, H. Pang, A. Georgiadis, and C. Cecati, "Wireless power transfer—An overview," *IEEE Trans. Ind. Electron.*, vol. 66, no. 2, pp. 1044–1058, Feb. 2019.

[6] J. Kim, D.-H. Kim, J. Choi, K.-H. Kim, and Y.-J. Park, "Free-positioning wireless charging system for small electronic devices using a bowl-shaped transmitting coil," *IEEE Trans. Microw. Theory Techn.*, vol. 63, no. 3, pp. 791–800, Mar. 2015.

[7] Y. Song, R. Boekraad, L. Roussos, A. Kooijman, C. Wang, and J. Geraedts, "3D printed electronics: Opportunities and challenges for industrial designers," in *Proc. Int. Design Eng. Tech. Conf. Comput. Inf. Eng. Conf.*, Cleveland, OH, USA, Aug. 2017, pp. 1–11.

[8] M. Zargham and P. G. Gulak, "Maximum achievable efficiency in near-field coupled power-transfer systems," *IEEE Trans. Biomed. Circuits Syst.*, vol. 6, no. 3, pp. 228–245, Jun. 2012.

[9] A. A. Eteng, S. K. Abdul Rahim, C. Y. Leow, B. W. Chew, and G. A. E. Vandenbosch, "Two-stage design method for enhanced inductive energy transmission with Q-constrained planar square loops," *PLOS ONE*, vol. 11, no. 2, Feb. 2016, Art. no. e0148808.

[10] D. Van Wageningen and T. Staring, "The Qi wireless power standard," in *Proc. 14th Int. Power Electron. Motion Control Conf. EPE-PEMC*, Ohrid, Macedonia, Sep. 2010, pp. 25–32.

[11] A. Rakhymbay, A. Khamitov, M. Bagheri, B. Alimkhanuly, M. Lu, and T. Phung, "Precise analysis on mutual inductance variation in dynamic wireless charging of electric vehicle," *Energies*, vol. 11, no. 3, p. 624, Mar. 2018.

[12] Z. Luo and X. Wei, "Analysis of square and circular planar spiral coils in wireless power transfer system for electric vehicles," *IEEE Trans. Ind. Electron.*, vol. 65, no. 1, pp. 331–341, Jan. 2018.

[13] R. Lemdiasov and A. Venkatasubramanian, "Transmit coil design for Wireless Power Transfer for medical implants," in *Proc. 39th Annu. Int. Conf. IEEE Eng. Med. Biol. Soc. (EMBC)*, Seogwipo, South Korea, Jul. 2017, pp. 2158–2161.

[14] N. Ha-Van and C. Seo, "Analytical and experimental investigations of omnidirectional wireless power transfer using a cubic transmitter," *IEEE Trans. Ind. Electron.*, vol. 65, no. 2, pp. 1358–1366, Feb. 2018.

[15] A. E. Rendon-Nava, J. A. Díaz-Méndez, L. Nino-de-Rivera, W. Calleja-Arriaga, F. Gil-Carrasco, and D. Díaz-Alonso, "Study of the effect of distance and misalignment between magnetically coupled coils for wireless power transfer in intraocular pressure measurement," *Sci. World J.*, vol. 2014, Jul. 2014, Art. no. 692434.

[16] T. Hou, Y. Song, W. S. Elkhuizen, J. Jiang, and J. M. P. Geraedts, "3D wireless power transfer based on 3D printed electronics," in *Proc. IEEE 14th Int. Conf. Automat. Sci. Eng. (CASE)*, Munich, Germany, Aug. 2018, pp. 499–505.

[17] W. G. Hurley and M. C. Duffy, "Calculation of self- and mutual impedances in planar sandwich inductors," *IEEE Trans. Magn.*, vol. 33, no. 3, pp. 2282–2290, May 1997.

[18] S. R. Khan and G. Choi, "Analysis and optimization of four-coil planar magnetically coupled printed spiral resonators," *Sensors*, vol. 16, no. 8, p. 1219, Aug. 2016.

[19] C. L. W. Sonntag, E. A. Lomonova, and J. L. Duarte, "Implementation of the Neumann formula for calculating the mutual inductance between planar PCB inductors," in *Proc. 18th Int. Conf. Elect. Mach.*, Vilamoura, Portugal, Sep. 2008, pp. 1–6.

[20] P. L. F. Penalver, C. L. C. Torriente, E. da Silva Braga, M. A. R. Alves, P. H. Roesler, and J. F. Mologni, "Pseudo-analytical model for calculation of flat circular inductors with rectangular cross-section," *Microelectron. J.*, vol. 78, pp. 46–53, Aug. 2018.

[21] H. Tavakkoli, E. Abbaspour-Sani, A. Khalilzadegan, A.-M. Abazari, and G. Rezazadeh, "Mutual inductance calculation between two coaxial planar spiral coils with an arbitrary number of sides," *Microelectron. J.*, vol. 85, pp. 98–108, Mar. 2019.

[22] K. Ishida, T. Itaya, A. Tanaka, N. Takehira, and T. Miki,, "Arbitrary-shaped single-layer coil self-inductance using shape functions," *IET Sci. Meas. Technol.*, vol. 5, no. 1, pp. 21–27, Jan. 2011.

[23] K. Ishida, T. Itaya, A. Tanaka, and N. Takehira, "Magnetic field analysis of an arbitrary shaped coil using shape functions," *IEEE Trans. Magn.*, vol. 45, no. 1, pp. 104–112, Jan. 2009.

[24] K. Budnik and W. Machczyński, "Magnetic field of complex helical conductors," *Arch. Electr. Eng.*, vol. 62, no. 4, pp. 533–540, Dec. 2013.

[25] T. Tominaka, "Self- and mutual inductances of long coaxial helical conductors," *Supercond. Sci. Technol.*, vol. 21, no. 1, Jan. 2008, Art. no. 015011.

[26] T. Tominaka, "Inductance calculation of twisted conductors by the broken line approximation," *Cryogenics*, vol. 49, no. 2, pp. 94–102, Feb. 2009.

[27] C. D. Sijoy and S. Chaturvedi, "Fast and accurate inductance calculations for arbitrarily—wound coils for pulsed power applications," in *Proc. IEEE Pulsed Power Conf.*, Mouterey, CA, USA, Jun. 2005, pp. 1464–1467.

[28] C. Volkmar, T. Baruth, J. Simon, U. Ricklefs, and R. Thueringer, "Arbitrarily shaped coils' inductance simulation based on a 3-dimensional solution of the Biot-Savart law," in *Proc. 36th Int. Spring Seminar Electron. Technol.*, Alba Iulia, Romania, May 2013, pp. 210–215.

[29] M. Mahto and B. Sniderman. (2017). *3D Opportunity for Electronics Additive Manufacturing Powers Up*. Accessed: Feb. 25, 2019. [Online]. Available: https://www2.deloitte.com/insights/us/en/focus/3d-opportunity/additive-manufacturing-3d-printed-electronics.html
[30] Voxel8. (2018). *3D Electronics Printer VOXEL8*. Accessed: Jan. 7, 2019. [Online]. Available: https://3dprint.com/35085/voxel8-electronics-3d-printer/
[31] D. Cadman, S. Zhang, and Y. Vardaxoglou, "Fused deposition modelling for microwave circuits & antennas," in *Proc. Int. Symp. Antennas Propag. (ISAP)*, Okinawa, Japan, Oct. 2016, pp. 418–419.
[32] E. Jabari and E. Toyserkani, "Aerosol-Jet printing of highly flexible and conductive graphene/silver patterns," *Mater. Lett.*, vol. 174, pp. 40–43, Jul. 2016.
[33] ChemCubedLLC. (2018). Accessed: Jun. 26, 2019. *Multi-Layer/Multi-Material Digital Printing Solutions for Electronics*. [Online]. Available: https://www.chemcubed.com/electrojet
[34] N. Dimension. (2019). *Precision Additive Manufacturing of Printed Electronics*. Accessed: Jun. 6 2019. [Online]. Available: https://www.nano-di.com/dragonfly-pro-3d-printer
[35] P. S. Karthik and S. P. Singh, "Conductive silver inks and their applications in printed and flexible electronics," *RSC Adv.*, vol. 5, no. 95, pp. 77760–77790, 2015.
[36] S. A. Odom, S. Chayanupatkul, B. J. Blaiszik, O. Zhao, A. C. Jackson, P. V. Braun, N. R. Sottos, S. R. White, and J. S. Moore, "A self-healing conductive ink," *Adv. Mater.*, vol. 24, no. 19, pp. 2578–2581, May 2012.
[37] Voxel8. (2016). *Silver Conductive Ink Technical Data Sheet*. Accessed: Jun. 29, 2019. [Online]. Available: https://p4.zdassets.com/hc/theme_assets/638849/200059206/Silver_Ink_Standard_TDS.pdf
[38] J. J. Adams, E. B. Duoss, T. F. Malkowski, M. J. Motala, B. Y. Ahn, R. G. Nuzzo, J. T. Bernhard, and J. A. Lewis, "Conformal printing of electrically small antennas on three-dimensional surfaces," *Adv. Mater.*, vol. 23, no. 11, pp. 1335–1340, Mar. 2011.
[39] F. Wang, P. Mao, and H. He, "Dispensing of high concentration Ag nanoparticles ink for ultra-low resistivity paper-based writing electronics," *Sci. Rep.*, vol. 6, no. 1, Aug. 2016, Art. no. 21398.
[40] E. Balliu, H. Andersson, M. Engholm, T. Öhlund, H.-E. Nilsson, and H. Olin, "Selective laser sintering of inkjet-printed silver nanoparticle inks on paper substrates to achieve highly conductive patterns," *Sci. Rep.*, vol. 8, no. 1, Jul. 2018, Art. no. 10408.
[41] Demcon. (2018). *The World's First Multi-Metal Printer*. Accessed: Feb. 25, 2019. [Online]. Available: https://www.demcon.nl/en/showcase/the-worlds-first-multi-metal-printer/
[42] S. Jeong, J. Song, H. Kim, S. Lee, J. Kim, J. Lee, Y. Kim, S. Kim, and J. Song, "Design and analysis of wireless power transfer system using flexible coil and shielding material on smartwatch strap," in *Proc. IEEE Wireless Power Transf. Conf. (WPTC)*, Taipei, Taiwan, May 2017, pp. 1–3.
[43] S. Jeong, "Smartwatch strap wireless power transfer system with flexible PCB coil and shielding material," *IEEE Trans. Ind. Electron.*, vol. 66, no. 5, pp. 4054–4064, May 2019.
[44] V. Iyer, J. Chan, and S. Gollakota, "3D printing wireless connected objects," *ACM Trans. Graph.*, vol. 36, no. 6, p. 242, Nov. 2017.
[45] D. Espalin, D. W. Muse, E. MacDonald, and R. B. Wicker, "3D printing multifunctionality: Structures with electronics," *Int. J. Adv. Manuf. Technol.*, vol. 72, nos. 5–8, pp. 963–978, 2014.
[46] E. Macdonald, R. Salas, D. Espalin, M. Perez, E. Aguilera, D. Muse, and R. B. Wicker, "3D printing for the rapid prototyping of structural electronics," *IEEE Access*, vol. 2, pp. 234–242, 2014.
[47] E. MacDonald and R. Wicker, "Multiprocess 3D printing for increasing component functionality," *Science*, vol. 353, no. 6307, Sep. 2016, Art. no. aaf2093.
[48] H. Ota, Y. Gao, A. Zhao, E. Wu, S. Challa, K. Chen, H. M. Fahad, A. K. Jha, D. Kiriya, W. Gao, H. Shiraki, K. Morioka, A. R. Ferguson, K. E. Healy, R. W. Davis, and A. Javey, "Application of 3D printing for smart objects with embedded electronic sensors and systems," *Adv. Mater. Technol.*, vol. 1, no. 1, Apr. 2016, Art. no. 1600013.
[49] X. Yu, K. Moez, I.-C. Wey, and J. Chen, "Power management design for lab-on-chip biosensors," in *Proc. 38th Annu. Int. Conf. IEEE Eng. Med. Biol. Soc. (EMBC)*, Orlando, FL, USA, Aug. 2016, pp. 2986–2989.
[50] Z. Zhu, S.-Z. Guo, T. Hirdler, C. Eide, X. Fan. J. Tolar, and M. C. McAlpine, "3D printed functional and biological materials on moving freeform surfaces," *Adv. Mater.*, vol. 30, no. 23, Jun. 2018, Art. no. 1707495.
[51] N. Lazarus, S. S. Bedair, and G. L. Smith, "Creating 3D printed magnetic devices with ferrofluids and liquid metals," *Additive Manuf.*, vol. 26, pp. 15–21, Mar. 2019.
[52] L. Piegl and W. Tiller, *The NURBS Book*, 2nd ed. Berlin, Germany: Springer-Verlag, 2012, pp. 117–139.
[53] P. S. Heckbert, "Survey of texture mapping," *IEEE Comput. Graph. Appl.*, vol. 6, no. 11, pp. 56–67, Nov. 1986.
[54] F. W. Grover, *Inductance Calculations*. New York, NY, USA: Courier Corp., 2013, pp. 179–211.
[55] M. Q. Nguyen, D. Plesa, S. Rao, and J.-C. Chiao, "A multi-input and multi-output wireless energy transfer system," in *Proc. IEEE MTT-S Int. Microw. Symp. (IMS)*, Tampa, FL, USA, Jun. 2014, pp. 1–3.
[56] *Standard Test Methods for Measuring Adhesion by Tape Test1*, Standard D3359-09, ASTM, 2009.
[57] J. Perzow. (2016). *Measuring Wireless Charging Efficiency in the Real World*. Accessed: Jun. 28, 2019. [Online]. Available: https://www.powerelectronictips.com/measuring-wireless-charging-efficiency-in-the-real-world/
[58] ANSYS. (2019). *ANSYS Maxwell Capabilities Low Frequency Electromagnetic Field Simulation*. Accessed: Jun. 25, 2019. [Online]. Available: https://www.ansys.com/products/electronics/ansys-maxwell/maxwell-capabilities
[59] C. Kim, D. Espalin, M. Liang, H. Xin, A. Cuaron, I. Varela, E. Macdonald, and R. B. Wicker, "3D printed electronics with high performance, multi-layered electrical interconnect," *IEEE Access*, vol. 5, pp. 25286–25294, 2017.
[60] K. Angel, H. H. Tsang, S. S. Bedair, G. L. Smith, and N. Lazarus, "Selective electroplating of 3D printed parts," *Additive Manuf.*, vol. 20, pp. 164–172, Mar. 2018.
[61] S. Hawasli, H. Tsang, N. Lazarus, G. Smith, and E. Forsythe, "Improving conductivity of 3D printed conductive pastes for RF & high performance electronics," in *Proc. IEEE MTT-S Int. Microw. Workshop Adv. Mater. Processes RF THz Appl. (IMWS-AMP)*, Ann Arbor, MI, USA, Jul. 2018, pp. 1–3.
[62] L. C. Yung, C. C. Fei, J. Mandeep, H. Binti Abdullah, and L. K. Wee, "Synthesis of a nano-silver metal ink for use in thick conductive film fabrication applied on a semiconductor package," *PLoS ONE*, vol. 9, no. 5, May 2014, Art. no. e97484.
[63] Y.-I. Lee and Y.-H. Choa, "Adhesion enhancement of ink-jet printed conductive copper patterns on a flexible substrate," *J. Mater. Chem.*, vol. 22, no. 25, May 2012, Art. no. 12517.
[64] Y. Wang, F. Castles, and P. S. Grant, "3D Printing of NiZn ferrite/ABS magnetic composites for electromagnetic devices," *MRS Proc.*, vol. 1788, pp. 29–35, Jul. 2015.

TAO HOU received the B.S. degree in mechatronics engineering from Shanghai University, China, in 2013, where he started his successive master doctor program. He is currently an exchange Ph.D. candidate with the Delft University of Technology. His current research interests include 3D wireless power transfer and 3D printed electronics.

JUN XU received the M.S. degree in biomedical engineering from Shanghai University, China, in 2018, where he started his doctor program. He is currently pursuing the Ph.D. degree with the Delft University of Technology. His current research interest includes 3D printed electronics.

WILLEMIJN S. ELKHUIZEN received the bachelor's and master's degrees from Industrial Design Engineering, Delft. In 2013, sponsored by Océ, she started her Ph.D. research on 3D printing and fine art reproduction.

CHARLIE C. L. WANG is currently a Professor with the Department of Mechanical and Automation Engineering, The Chinese University of Hong Kong. He is a Fellow of American Society of Mechanical Engineers (ASME). His research interests include geometric computing, computational design, advanced manufacturing, and robotics.

JIEHUI JIANG received the Ph.D. degree in design engineering from the Delft University of Technology, the Netherlands. He is currently an Associate Professor with the Institute of Biomedical Engineering, School of Communication and Information Engineering, Shanghai University. His research interest includes medical device development.

JO M. P. GERAEDTS received the Ph.D. degree in physics from the Radboud University of Nijmegen, in 1983. He joined Océ-van der Grinten N.V., in 1983, and from 2008, he was appointed the Chair of Mechatronics Design, Faculty of Industrial Design Engineering, Delft University of Technology. Since then, he built step by step a new research environment into 3D multi-modal scanning, 3D multi-material printing, and human-robot interaction.

YU (WOLF) SONG received the Ph.D. degree from the Department of Mechanical Engineering, The University of Hong Kong. He joined Faculty of Industrial Design Engineering, Delft University of Technology in 2001 as a Research Fellow. He is currently an Associate Professor with the Department of Design Engineering. His main research interests include 3D printed electronics, 3D scanning, and ergonomics.